Earth and Planetary Science Letters 565 (2021) 116955

Contents lists available at ScienceDirect

Earth and Planetary Science Letters

www.elsevier.com/locate/epsl

The Water-Fe-Pressure dependent single-crystal elastic properties of wadsleyite: Implications for the seismic anisotropy in the upper Mantle Transition Zone

Wen-Yi Zhou [a,b], Zhiyuan Ren [a], Jin S. Zhang [a,b,*], Bin Chen [c], Ming Hao [a,b], Tomohiro Ohuchi [d], Lowell Miyagi [e], Dongzhou Zhang [c,f], Esen E. Alp [g], Barbara Lavina [g], Brandon Schmandt [a]

[a] Department of Earth and Planetary Sciences, University of New Mexico, Albuquerque, NM, USA
[b] Institute of Meteoritics, University of New Mexico, Albuquerque, NM, USA
[c] Hawaii Institute of Geophysics and Planetology, University of Hawai'i at Mānoa, Honolulu, HI, USA
[d] Geodynamics Research Center, Ehime University, Matsuyama, Japan
[e] Department of Geology and Geophysics, University of Utah, Salt Lake City, UT, USA
[f] GeoSoilEnviroCARS, University of Chicago, Argonne National Laboratory, Argonne, IL, USA
[g] Sector 3, Advanced Photon Source, Argonne National Laboratory, Argonne, IL, USA

ARTICLE INFO

Article history:
Received 13 November 2020
Received in revised form 3 April 2021
Accepted 14 April 2021
Available online xxxx
Editor: J. Badro

Keywords:
wadsleyite
elasticity
seismic anisotropy
Mantle Transition Zone
water sensor

ABSTRACT

Recent seismic studies suggested an anisotropic Mantle Transition Zone (MTZ) in areas adjacent to subducted slabs. Wadsleyite is the main anisotropy contributor in the upper MTZ, therefore the interpretation of these seismic observations requires the knowledge of single-crystal elastic moduli ($C_{ij}s$) and the deformation-induced lattice preferred orientation (LPO) of wadsleyite. Wadsleyite can host up to 3 wt% water in its crystal structure as point defects in the form of hydroxyl groups, however, the combined effect of water content, Fe content, and pressure on the $C_{ij}s$ of wadsleyite remains unclear. In this study, we measured the high-pressure single-crystal elasticity of a synthetic hydrous Fe-bearing wadsleyite (0.14 (4) wt% water, Fe#=9.4, $Fe^{3+}/\Sigma Fe$=0.3) up to 18.2 (2) GPa. In combination with previous experimental data, we separated the effects of pressure, water, and Fe contents on the $C_{ij}s$ and intrinsic elastic anisotropy of wadsleyite. Our results suggest that the intrinsic elastic anisotropy of wadsleyite decreases with pressure, water, and Fe contents. At 15 GPa, increasing the water content by 0.1 wt% or Fe# by 1 decreases the V_P and V_S anisotropy of wadsleyite by ~1.1-1.3%, and ~0.8-1.3% in average, respectively. Combining the LPO determined in previous deformation experiments, we modeled the seismic anisotropy in the upper MTZ generated by a sub-vertical mantle flow near cold subducted slabs and a sub-horizontal mantle flow in the ambient mantle. In both scenarios, the LPO of wadsleyite leads to V_{SV} (vertically polarized shear wave velocity) > V_{SH} (horizontally polarized shear wave velocity). Our results suggest that wadsleyite may account for a weak anisotropic MTZ (<1%) on the global scale. Considering the fact that water decreases the elastic anisotropy but promotes LPO of wadsleyite, seismic anisotropy may not be a good water sensor in the upper MTZ.

1. Introduction

The existence and magnitude of radial and azimuthal anisotropy in the Mantle Transition Zone (MTZ, ~410-660 km depth) on the global scale is highly controversial. A study using long-period surface wave overtones by Yuan and Beghein (2013) suggested that ~1% anisotropy is common throughout the MTZ, whereas other path integrated shear-wave splitting data are more consistent with the seismic anisotropy restricted to the upper mantle down to ~300 km (Savage, 1999). Many lines of evidence suggested that the seismic anisotropy of MTZ can be strong in the localized regions adjacent to some subducting slabs (Foley and Long, 2011; Chang and Ferreira, 2019; Huang et al., 2019). Interpretation of these global and local anisotropic seismic observations requires

* Corresponding author at: Department of Earth and Planetary Sciences, University of New Mexico, Albuquerque, NM, USA.
E-mail address: jinzhang@unm.edu (J.S. Zhang).

https://doi.org/10.1016/j.epsl.2021.116955
0012-821X/

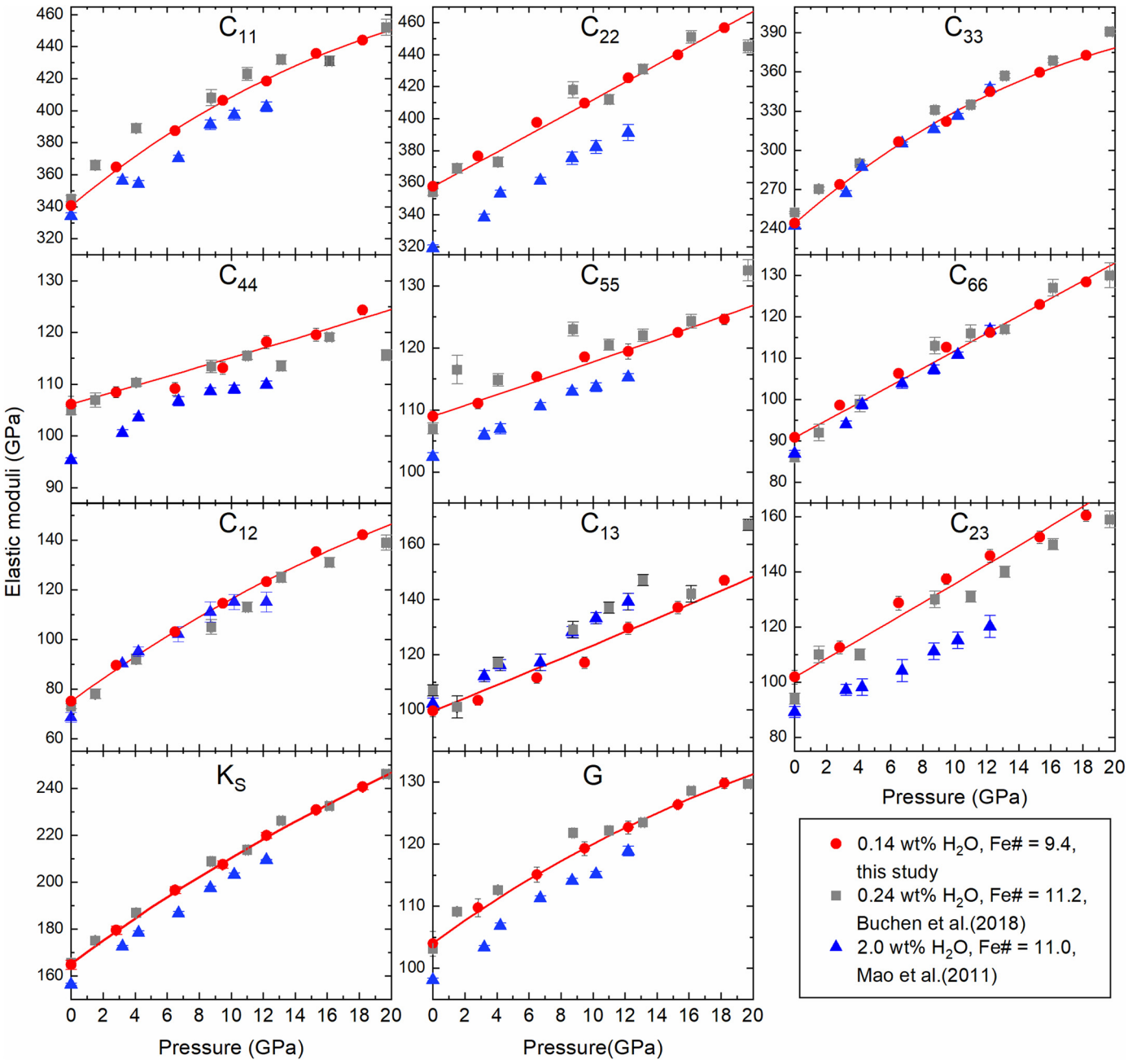

Fig. 1. C_{ij}s, K_S, and G of three different hydrous Fe-bearing wadsleyite samples as a function of pressure. Solid lines represent 3rd or 4th order finite strain EOS fitting results for the wadsleyite sample measured in this study. VRH averaging scheme is used to calculate the Ks and G of isotropic polycrystalline aggregates in this study.

knowledge of the anisotropic elastic properties of relevant MTZ minerals.

Compared with other MTZ minerals, wadsleyite, which constitutes 50-60 vol% in pyrolite, is the major anisotropy contributor in the upper MTZ (~410-520 km depth). Garnet is nearly elastically isotropic (Jiang et al., 2004), and elastically anisotropic clinopyroxene only constitutes <10 vol.% at ~410 km depth and may completely dissolve into the garnet structure at ~500 km (Frost, 2008). As a result, lattice preferred orientation (LPO) of anisotropic wadsleyite under high pressure-temperature conditions is the most viable explanation for the seismic anisotropy observed in the upper MTZ.

Wadsleyite can host up to 3 wt% water (exists as hydroxyl in crystal structure instead of molecular water, Inoue et al., 1995) and its single-crystal elastic properties at high-pressure conditions have been determined in several previous studies. Hydrous Fe-bearing wadsleyite with different Fe and water contents were measured up to ~12 GPa and ~20 GPa by Mao et al. (2011) and Buchen et al. (2018), respectively (Fig. 1), whereas anhydrous Fe-bearing wadsleyite was measured up to ~18 GPa by Wang et al. (2014) (Fig. 2). Buchen et al. (2018) modeled the combined effects of Fe# ($100^{*}Fe_{mol}/(Fe_{mol}+Mg_{mol})$) and water on the isotropic aggregate sound wave velocities of wadsleyite based on experimental data. First-principal calculation has also been employed to study the effect of Fe# on the single-crystal elastic properties of wadsleyite (Núñez-Valdez et al., 2011). However, the combined influences of water content, Fe#, and pressure on the single-crystal elastic properties and thus elastic anisotropy of wadsleyite remain poorly constrained. The strong softening of C_{44} and C_{12} inferred from the finite strain equation of state derived in Mao et al. (2011) was not observed by Buchen et al. (2018). As pointed out in Zhang et al. (2018), the softening of C_{44} and C_{12}, if true, would result

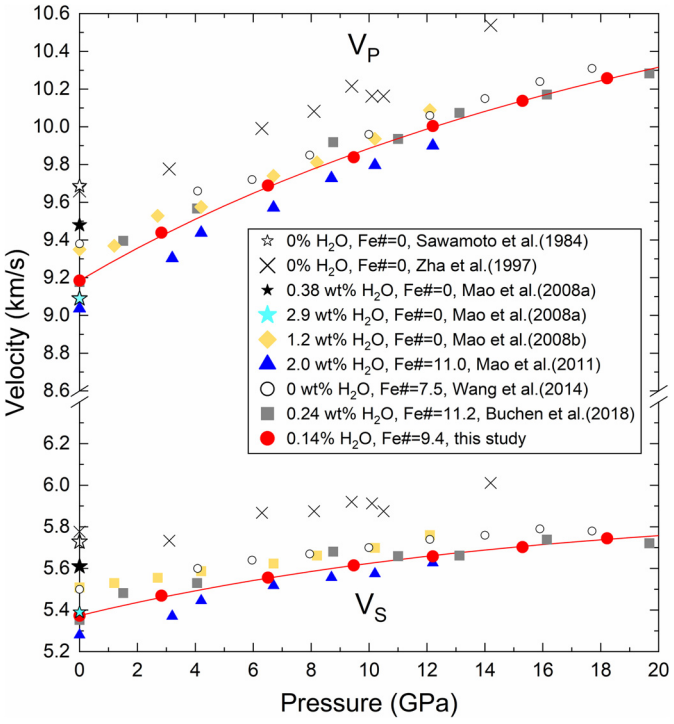

Fig. 2. Experimentally determined V_P and V_S of isotropic polycrystalline wadsleyite aggregates from single-crystal Brillouin spectroscopy experiments compiled and utilized in this study. The water contents of wadsleyite samples in Mao et al. (2008a, 2008b) and Mao et al. (2011) were updated to values re-examined by Chang et al. (2015). Solid lines represent the 4th order finite strain EOS fitting results for the wadsleyite sample measured in this study calculated from the best-fit $C_{ij}s$ model under VRH averaging scheme.

in a strong increase of elastic anisotropy of wadsleyite at the MTZ depth range and potentially create detectable seismic signatures of anisotropy. Therefore, new measurements on hydrous Fe-bearing wadsleyite, in particular, the modeling of water-Fe-pressure effects using all the available single-crystal experimental data is needed to clarify this issue.

Wadsleyite can develop several different deformation-induced LPOs at 15-17 GPa under relatively low stress (<1 GPa), and the exact type depends on both the water content and temperature: Under normal upper MTZ temperatures, type I [0 0 1] (0 1 0) and type II [0 0 1] (1 0 0) dominate when water contents are <0.05 wt% and >0.05 wt%, respectively; Under cold conditions (1550-1720 K), type III [1 0 0] (0 0 1) LPO develops (Ohuchi et al., 2014).

In this study, we determined the single-crystal elasticity of a new hydrous Fe-bearing wadsleyite sample up to 18.2 (2) GPa by Brillouin spectroscopy, and then performed systematic analysis based on all the available experimental data to separate the effects of water, Fe, and pressure on the single-crystal elasticity of wadsleyite. Finally, we combined the water-Fe-pressure dependent single-crystal elastic moduli ($C_{ij}s$) of wadsleyite with different deformation-induced LPOs determined in Ohuchi et al. (2014) to estimate the seismic anisotropy under different flow fields in the MTZ and compared it with seismic observations.

2. Methods

2.1. Sample synthesis and characterization

The hydrous Fe-bearing wadsleyite crystals were synthesized using the COMPRES 10/5 assembly in a 1000-ton Multi-Anvil Press at the University of Hawai'i at Mānoa (UHM). We packed and sealed the small San Carlos olivine crystals with deionized water into a gold capsule. The crystals were synthesized at 1673 K and 16 GPa with a duration of 24 hours. The sizes of wadsleyite crystals in the run product range from 50 μm to 100 μm.

We measured the water weight content (wt%) of 9 wadsleyite platelets using the Thermal Fisher Nicolet Nexus 670 Fourier Transformed Infrared Spectrometer (FTIR) at the University of New Mexico (UNM). The narrow-band mercury-cadmium-telluride detector was cooled by liquid nitrogen before starting measurements. The unpolarized spectra with wavenumber ranging from 1500 to 4800 cm^{-1} were acquired by an IR light source and a CaF_2 beam splitter. The average water content for the synthetic wadsleyite is 0.14 (4) wt.% (see Supplementary Materials, Fig. S1 for details). We obtained the chemical composition of the synthetic wadsleyite sample by the Electron Probe Micro-Analysis (EPMA) using the JEOL 8200 Electron Microprobe facility at UNM (Table S1). The accelerating voltage is 15 kV and the beam current is 20 nA. The main element standards were Forsterite for Mg and Si, and Almandine for Fe. We also measured the $Fe^{3+}/\Sigma Fe$ of the synthetic wadsleyite samples using the Mössbauer spectrometer at the offline Mössbauer spectroscopy laboratory at sector 3, Advanced Photon Source (APS) in the Argonne National Laboratory (ANL). The data was obtained using constant acceleration mode, with a ^{57}Co/Pd source of approximately 5 mCi strength. Vortex silicon drift detector with an energy resolution of 150 eV at 14.4 keV was used to reduce the background. The data was analyzed using WinNormos (WISSEL Co.) program. The transmission Mössbauer spectrum of our sample is shown in Fig. S2. A two-site model corresponding to Fe^{2+} and Fe^{3+} hyperfine parameter values was used. Fe^{2+} site has an isomer shift of 1.04 mm/s, and quadrupole splitting of 2.6 mm/s. The Fe^{3+} site, on the other hand, has an isomer shift value of 0.36 mm/s and quadrupole splitting of 0.88 mm/s. These valence assignments are consistent with the literature values for 6-fold coordinated Fe (Dyar et al., 2006). The final chemical formula of the sample is determined as $Mg_{1.788}Fe^{2+}_{0.131}Fe^{3+}_{0.056}Al_{0.003}Mn_{0.003}Ni_{0.007}H_{0.022}Si_{0.986}O_4$ (Fe#=9.4(2)).

We polished 6 wadsleyite single crystals into thin platelets with size ~50 μm × 50 μm × 12 μm for single-crystal X-ray Diffraction experiments. These platelets are without scratches and inclusions after examination under a high magnification petrographic microscope. The unit cell parameters and orientations of the 6 polished wadsleyite crystals were determined by the single-crystal XRD experiments at 1) the GeoSoilEnviroCars (GSECARS) experimental station 13-BM-C at APS in ANL and 2) the X-ray Atlas Diffraction Lab at UHM. At 13-BM-C, the X-ray beam was monochromated to 28.6 keV (0.434 Å) with 1 eV bandwidth. A Kirkpatrick-Baez mirror system was used to obtain a vertical × horizontal focus spot size of 12 μm × 18 μm, measured as full width at half maximum (FWHM). The MAR165 detector (Rayonix) was placed about 175 mm away from the sample, and LaB_6 powder at ambient conditions was used to calibrate the distance and tilting of the detector. The crystals were placed on a glass slide, we found that the tilting of the samples and glass slide was minimal by examining the laser beam reflected at the polished crystal surfaces and glass slide with 0° incident angle. The diffraction patterns were collected in the φ-scan geometry for a φ angle range of ± 23° with 1° step and 1 second exposure per frame. ATREX software package was used to extract the unit cell parameters and the orientation of each crystal. At the X-ray Atlas Lab, diffraction measurements were carried out on a customized Bruker D8 Venture diffractometer with a Phonon II detector, fixed-chi goniometer and Incoatec IμS 3.0 Ag Kα microfocus source with Helios focusing optics. Similar φ-scan geometry was used for the diffraction and the exposure time was 20 seconds per frame, and the Bruker APEX3 software was used to extract the lattice parameters. The ambient density (ρ_0) was calculated as 3.595(6) g/cm^3 based on the unit cell parameters of a=5.711(2) Å, b=11.453(6) Å, c=8.268(7) Å. To

better constrain the 9 independent $C_{ij}s$, we performed a sensitivity test (see Supplementary Materials) to choose the best combination of crystal orientations for Brillouin measurements. The plane normals of the 3 crystals we selected are (-0.3420 0.8718 0.3506), (-0.1013 -0.4397 0.8924), and (0.5341 0.0953 -0.8401) in the Cartesian coordinates. The angular uncertainties of the measured plane normals are within 0.5°, propagating to a velocity measurement uncertainty of <15 m/s, which is well under the Brillouin measurement precision of 30 m/s.

2.2. High-pressure Brillouin spectroscopy experiments and data analysis procedure

We used BX90 Diamond Anvil Cells (DAC) to generate high-pressure conditions. The slow directions of the two diamonds were pre-oriented to match each other. Rhenium gaskets were indented using the 350 μm-culet diamonds and 250 μm-diameter holes were drilled to create the sample chambers. The sample was loaded with two ruby spheres which acted as the pressure standards. A neon pressure-transmitting medium was gas-loaded into the sample chamber at GSECARS, APS, ANL. As part of the alignment process, we examined the tilting and non-parallelism of the sample and the diamonds in the DAC using the laser beam reflected at the polished crystal surfaces and diamond tables with 0° incident angle. The reflected laser beams match each other nicely, suggesting that the tilting and non-parallelism were minimal. The Brillouin spectroscopy experiments were performed at the Laser Spectroscopy Lab at UNM. A 532 nm single-mode diode-pumped solid-state laser was used as the light source for the Brillouin experiments. We used a 50° symmetric forward scattering geometry. Before the experiment, the scattering angle of the system was calibrated to be 50.47(8)° using a standard silica glass Corning 7980. A 6-pass tandem Fabry-Pérot interferometer was used to measure the Brillouin frequency shift. At each pressure condition, we measured the compressional wave (P-Wave) velocity (V_P) and shear wave (S-Wave) velocities (V_S) of the crystals every 15° along the 360° azimuth (Chi angles at 0, 15, 30, 45, 60, 75, 90, 105, 120, 135, 150, 165, 180, 195, 210, 225, 240, 255, 270, 285, 300, 315, 330, 345). The typical spectrums are shown in Fig. S4.

Given a starting $C_{ij}s$ model of wadsleyite, we calculated a set of phonon directions of each Brillouin measurement after fixing the plane normals for the selected three crystals. Based on the calculated phonon direction–measured V_P, V_S data set, we then calculated the best-fit $C_{ij}s$ model through a least-square inversion of the Christoffel equation (Speziale and Duffy, 2002). Afterwards, we recalculated the phonon directions of each measurement based on this newly obtained best-fit $C_{ij}s$ model. The recalculated phonon directions and the velocities were used as the input again to calculate an updated $C_{ij}s$ model for another round. This process was repeated2-3 times until the difference in root-mean-square (RMS) residuals of two successive runs is smaller than 0.1 m/s. We assigned an assumed density (ρ) in the starting $C_{ij}s$ model to fit the high-pressure phonon direction–measured V_P, V_S data set, thus the inverted high-pressure $C_{ij}s$ at this step are not the best-fit values and will need to be updated with the best-fit high-pressure ρ in a later step. However, based on these obtained high-pressure $C_{ij}s$ with assumed ρ, we can calculate the best-fit K_S/ρ, G/ρ, thus V_P and V_S of wadsleyite aggregates under Voigt-Reuss-Hill (VRH) averaging scheme (Hill, 1963). The aggregate velocities are independent of the assumed high-pressure ρ and only depend on the experimentally measured velocities along different crystallographic directions (Zhang and Bass, 2016). We can then utilize the 4th order finite strain equation of state (EOS) (Equations S3-S20) to fit the lab-measured pressure-V_P-V_S data to derive $K_{S0}{}'$ ($\partial K_{S0}/\partial P$), $K_{S0}{}''$ ($\partial^2 K_{S0}/\partial P^2$), G_0' ($\partial G_0/\partial P$), and G_0''($\partial^2 G_0/\partial P^2$) with fixed lab-measured ρ_0, K_{S0}, and G_0 (0 in the subscript represents ambient-condition) (Davies and Dziewonski, 1975), as well as the best-fit high-pressure ρ. Finally, we updated the $C_{ij}s$, K_S, and G at each high pressure with the obtained best-fit high-pressure ρ.

2.3. Water-Fe-Pressure-elasticity modeling and anisotropy indices

To systematically study the effects of water, Fe, and pressure on the elasticity of wadsleyite, we compiled the water content, Fe#, ρ, and single-crystal elasticity data (K_S, G, $C_{ij}s$, V_P, and V_S) of 8 different wadsleyite samples under different pressure conditions (Sawamoto et al., 1984; Zha et al., 1997; Mao et al., 2008a, 2008b; Mao et al., 2011; Wang et al., 2014; Buchen et al., 2018; this study; Table S2). The 8 wadsleyite samples cover a wide range of water content (0-2.9 wt%) and Fe# (0-11.2), and 6 wadsleyite samples have been measured at high-pressure conditions including this study.

We adopted the following procedures to separate the effects of water, Fe, and pressure on the single-crystal elastic properties of wadsleyite:

(1) To reduce the number of fitting parameters, we firstly fit the ρ_0, K_{S0}, G_0, and each $C_{ij,0}$ of wadsleyite with respect to water contents (wt%) and Fe#, which was sufficiently simple to be described by an empirical linear relationship of $\boldsymbol{B}$= $\boldsymbol{B_0}$ + $\boldsymbol{B_1}$ × water (wt%) + $\boldsymbol{B_2}$ × Fe#;

(2) Given the ρ_0, K_{S0}, G_0, and $C_{ij,0}$ as well as their compositional dependence derived in step (1), the ambient thermoelastic properties of the 6 samples that have been measured at high-pressure conditions were fixed in the subsequent inversion process. After extensive testing (see Supplementary Materials), we chose to fit the $K_{S0}{}'$ and G_0' as compositional dependent with respect to water content or Fe#, and fix the $K_{S0}{}''$ and G_0'' to the values determined for the hydrous Fe-bearing wadsleyite measured in this study. We utilized 4th order finite strain EOS, and subsequently calculated the compositional dependence of each $C_{ij,0}{}'$ ($\partial C_{ij,0}/\partial P$) and $C_{ij,0}{}''$ ($\partial^2 C_{ij,0}/\partial P^2$). The equations utilized are shown in the Supplementary Materials as equations S3-S20.

To further verify the reliability of our inverted water-Fe-pressure dependent single-crystal elasticity model of wadsleyite, we compared the model-predicted values of $C_{ij}s$, K_S, G, V_P, and V_S at different pressures for all 8 wadsleyite samples with the experimentally determined values we compiled from previous studies (Table S3). The differences are mostly within 2% and 5% for aggregate elastic properties and $C_{ij}s$, respectively (Fig. 3). The pressure derivatives of the K_S, G, and $C_{ij}s$ calculated from our model are also consistent with the individually inverted values from our Brillouin experiments within uncertainty (Table S4). It is important to note that extrapolation to the composition and pressure range far beyond what has been experimentally investigated might lead to unreliable predictions. The accuracy of our modeling results can be improved with more high-pressure experimental data on wadsleyite in the future, especially those with water content higher than 2 wt%.

Buchen et al. (2017) has pointed out the possible effect of Fe^{3+} on the single-crystal elastic properties of wadsleyite. In this study, we chose to not separate the effect of Fe^{3+} from Fe^{2+} primarily due to the following 2 reasons: 1) Only 3 single-crystal sound velocity measurements exist for Fe-bearing wadsleyite with known Fe^{3+}/ ΣFe (Mao et al., 2011; Buchen et al., 2018, this study). With limited experimental data, it is difficult for us to separate the effects of Fe^{2+}, Fe^{3+}, pressure, and water together. 2) The calculated effects of Fe^{3+}/ΣFe =0.3 in our sample on its isothermal bulk modulus (1 GPa) and linear elastic moduli (3-5 GPa) at ambient condition are significantly smaller than the estimated uncertainties of the isothermal bulk modulus (2-49 GPa), and linear elastic moduli (7-464 GPa) for the 4-end members of wadsleyite given in Buchen et al. (2017). Although quantitative analysis on the effect of Fe^{3+} is

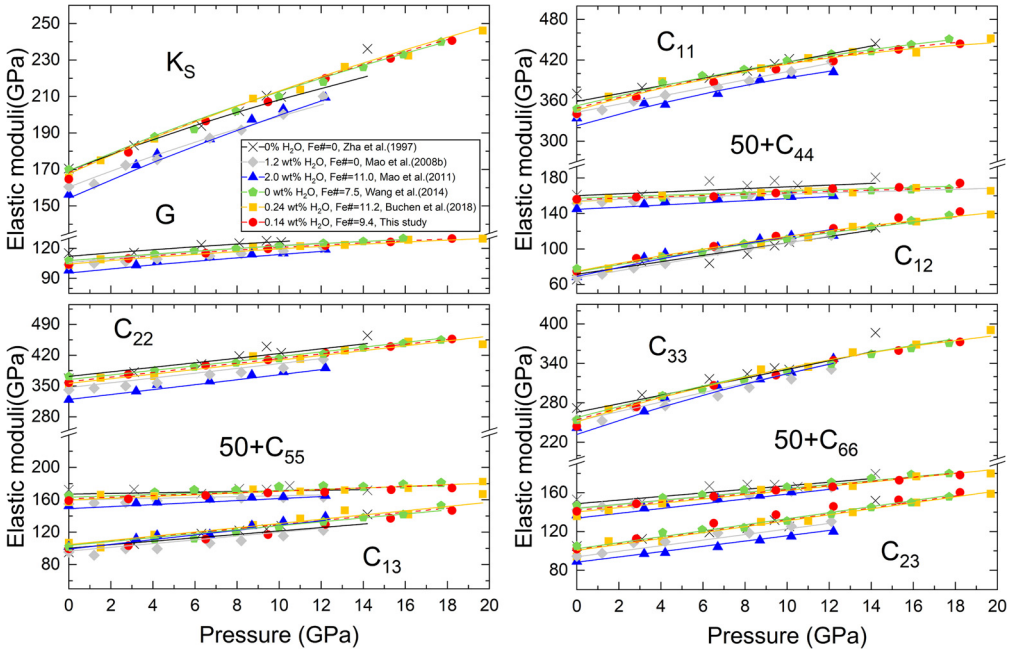

Fig. 3. Comparison between input Ks, G, C_{ij}s of wadsleyite (symbols) and model-predicted values (lines).

challenging based on the currently available experimental data, future studies on Fe-rich wadsleyite with higher Fe^{3+} concentration can help to further clarify this issue.

We finally derived the $C_{ij}s$, K_S, G, V_P, and V_S as well as several anisotropy indices in the parameter space spanned by typical water contents (0-3 wt% H_2O), Fe contents (Fe# 0-15), and relevant pressures (0-18 GPa) using the 4th order finite strain EOS.

The anisotropy indices we used are: Universal Anisotropy (A^U), which refers to the overall elastic anisotropy of minerals (Ranganathan and Ostoja-Starzewski, 2008). The superscripts R and V denote the Reuss and Voigt bounds of the homogeneous isotropic aggregate (Hill, 1963).

$$A^U = (5\frac{G^V}{G^R} + \frac{K_s^V}{K_s^R} - 6) * 100(\%)$$

V_P azimuthal anisotropy (A^{Vp}), which represents the maximum velocity difference of all V_P propagating along all directions, is defined as

$$A^{Vp} = \frac{Vp_{max} - Vp_{min}}{Vp_{max} + Vp_{min}} * 200(\%)$$

V_S azimuthal anisotropy (A^{Vs}), which represents the maximum difference of all V_S propagating along all directions, is defined as

$$A^{Vs} = \frac{Vs_{max} - Vs_{min}}{Vs_{max} + Vs_{min}} * 200(\%)$$

V_S radial anisotropy (D^{Vs}), which represents the maximum velocity difference between V_{S1} and V_{S2}, V_{S1} represents speed of fast S-Wave and V_{S2} represents speed of slow S-Wave propagating along the same direction but with different polarizations.

$$D^{Vs} = (\frac{|Vs_1 - Vs_2|}{Vs_1 + Vs_2})_{max} * 200(\%)$$

3. Results

3.1. Single-crystal elasticity of the hydrous Fe-bearing wadsleyite measured in this study

For the synthetic wadsleyite sample (0.14 wt% water, Fe#=9.4, $Fe^{3+}/\Sigma Fe$=0.3) measured in this study, using the data analysis procedure outlined in Section 2.2, we determined its K_{S0}, G_0, K_{S0}', K_{S0}'', G_0' and G_0'' as 165 (2) GPa, 104 (2) GPa, 5.2 (5), -0.16 (11) GPa^{-1}, 1.9 (2), and -0.076 (28) GPa^{-1}, respectively. The calculated aggregate elastic properties using the 4th order finite strain EOS based on these parameters match well with our experimentally determined values (Figs. 1, 2). The values of $C_{ij}s$ at each pressure in this study are listed in Table 1 and can be fit well using the 3rd or 4th order finite strain EOS (Fig. 1). The velocities predicted by the best-fit $C_{ij}s$ at high-pressure conditions match the experimentally measured velocities of the 3 wadsleyite crystals with RMS error less than 45 m/s (Fig. S5).

The softening of C_{44} and C_{12} starting at ~8 GPa inferred by the finite strain EOS reported in Mao et al. (2011) is not observed in our data (Fig. 1). In this study, $C_{44,0}$ is obtained as 106 (2) GPa with $\partial C_{44,0}/\partial P$ = 0.89 (5); $C_{12,0}$ is derived as 75 (1) GPa with $\partial C_{12,0}/\partial P$ = 4.8 (2) and $\partial C_{12,0}^2/\partial^2 P$ = -0.15 (2) GPa^{-1}.

3.2. The water-Fe-pressure dependent single-crystal elasticity model of wadsleyite

Based on the modeling method described in section 2.3, the compositional dependence of the ρ, K_{S0}, G_0, $C_{ij,0}$, and their pressure derivatives are listed in Table S5 and Table 2.

3.2.1. The effects of water, Fe, and pressure on $C_{ij}s$

Similar to olivine, water decreases all $C_{ij,0}$ in wadsleyite (Fig. S6, Table 2). The addition of 1 wt% water to Fe-free wadsleyite reduces its $C_{ij,0}$ by ~3-7%, whereas the reduction of $C_{ij,0}$ caused by the same amount of water for Fe-free olivine is only ~1-4% (Jacobsen et al., 2008). Among all the $C_{ij}s$ of wadsleyite at ambient condition, C_{22} and C_{23} are most sensitive to the water, whereas C_{12} and C_{13} are the least sensitive ones (Table 2). In comparison,

Table 1
C_{ij}s, K_S, G, V_P, and V_S for the hydrous Fe-bearing wadsleyite sample (0.14 wt% water, Fe#=9.4, $Fe^{3+}/\Sigma Fe$=0.3) measured in this study.

Pressure	1.0 atm	2.9(1) GPa	6.6(1) GPa	9.5(1) GPa	12.2(1) GPa	15.4(1) GPa	18.2(2) GPa
ρ (g/cm3)	3.595(6)	3.656	3.729	3.783	3.831	3.886	3.933
C_{11} (GPa)	341(1)	364(1)	387(1)	406(1)	418(1)	436(1)	444(1)
C_{22} (GPa)	358(1)	376(1)	397(1)	410(1)	425(2)	440(1)	457(1)
C_{33} (GPa)	244(2)	273(2)	307(2)	322(2)	345(2)	360(2)	373(2)
C_{44} (GPa)	106(2)	108(1)	109(1)	113(1)	118(1)	120(1)	124.3(9)
C_{55} (GPa)	109(1)	111(1)	115(1)	119(1)	119(1)	122.5(7)	124.6(9)
C_{66} (GPa)	90.8(7)	98.5(6)	106.3(7)	112.6(6)	116.1(8)	123.0(7)	128.4(5)
C_{12} (GPa)	75(1)	89(1)	103(1)	114(1)	123(1)	135(1)	142(1)
C_{13} (GPa)	99(2)	103(2)	112(2)	117(2)	129(2)	137(2)	147(2)
C_{23} (GPa)	102(3)	112(2)	129(2)	137(2)	146(2)	153(2)	160(2)
K_S^{VRH} (GPa)	165(2)	179(2)	197(1)	207(1)	220(1)	231(1)	241(1)
G^{VRH} (GPa)	104(2)	110(1)	115(1)	119(1)	123(1)	126(1)	130(1)
V_P (km/s)	9.19(3)	9.43(2)	9.69(2)	9.84(1)	10.00(1)	10.14(1)	10.26(1)
V_S (km/s)	5.38(3)	5.47(2)	5.56(2)	5.62(1)	5.66(1)	5.70(1)	5.75(1)

Table 2
Effects of adding 1 wt% water or increasing Fe# by 10 on the elastic properties of the dry Mg-endmember wadsleyite at 0 GPa and 300 K (one can calculate the effects of water or Fe for different wadsleyite samples based on the parameters listed in Table S5). "\" denotes that the influence is negligible.

	Add 1 wt% water	Increase Fe# by 10
$C_{11,0}$	↓ by 4%	↓ by 3%
$C_{22,0}$	↓ by 6%	↓ by 2%
$C_{33,0}$	↓ by 4%	↓ by 4%
$C_{44,0}$	↓ by 5%	↓ by 3%
$C_{55,0}$	↓ by 5%	↓ by 4%
$C_{66,0}$	↓ by 4%	↓ by 7%
$C_{12,0}$	↓ by 4%	↑ by 6%
$C_{13,0}$	↓ by 3%	↑ by 5%
$C_{23,0}$	↓ by 7%	\
K_{S0}	↓ by 4%	\
K_{S0}'	\	↑ by 13%
K_{S0}''	\	\
G_0	↓ by 5%	↓ by 5%
G_0'	↑ by 10%	\
G_0''	\	\

increasing Fe# of wadsleyite by 10 only decreases diagonal $C_{ij,0}$ by ~2-7% (Table 2).

Water in wadsleyite increases all $C_{ij,0}'$ except $C'_{23,0}$, Fe increases all $C_{ij,0}'$ except $C'_{44,0}$ and $C'_{23,0}$ (Table S5). Therefore, the high-pressure C_{ij} is determined by the two competing factors: Increasing water and Fe contents reduces $C_{ij,0}$ yet elevates $C_{ij,0}'$. Under the high-pressure condition of the upper MTZ (14-18 GPa, Fig. S6), water reduces C_{11}, C_{22}, C_{55} yet increases C_{23}; Fe reduces C_{11}, C_{44} yet increases C_{55}, C_{12}, C_{13}. Both C_{33} and C_{66} are relatively insensitive to the water and Fe contents. The modeling of the water and Fe effects on C_{44} and C_{12} further suggests that the strong softening of C_{44} and C_{12} at MTZ pressures, implied from the finite strain EOS derived in Mao et al. (2011), might be a fitting artifact, since the set of EOS in this study without showing such softening could fit the experimental data in Mao et al. (2011) reasonably well.

3.2.2. The effects of water, Fe, and pressure on K_S, G, V_P, and V_S

The incorporation of water in wadsleyite decreases both K_{S0} and $G_{0,}$ whereas increasing Fe# only decreases G_0 (Fig. 4, Table 2), which is consistent with previous studies (Mao et al., 2008a; Wang et al., 2014; Hazen et al., 2000).

Chang et al. (2015) found that water has no resolvable effect on pressure derivative of isothermal bulk modulus by performing high-pressure X-ray diffraction experiments on different hydrous wadsleyite crystals loaded in the same DAC. However, Buchen et al. (2018) suggested water increases K_{S0}' after comparing the K_{S0}' for their less hydrated wadsleyite with the K_{S0}' for a more hydrated sample measured in Mao et al. (2011). In this study, after removing the effect of Fe, our modeling results suggest that the increase of K_{S0}' caused by hydration is minimal. However, water in wadsleyite does increase G_0', so the softening effect of water on G is smaller at higher pressures while the effect of water on K_S persists to high pressure. On the other hand, increasing Fe# of wadsleyite would only increase K_{S0}' whereas it has no distinguishable effect on G_0', so the effect of Fe on G remains at high-pressure conditions. Interestingly, adding Fe increases K_S of wadsleyite at high-pressure conditions, possibly related to a stronger Fe-O bond than Mg-O bond, or stronger geometrical constraints after replacing Mg with Fe in the wadsleyite crystal structure under high pressure (Hazen et al., 2000; Buchen et al., 2017). In addition, the existence of Fe^{3+} rather than Fe^{2+} may soften the structure of wadsleyite along a axis under ambient condition (Buchen et al., 2017), although the modeling in the present study did not take the effect of valance state of Fe into account.

To summarize, at 14-18 GPa, water decreases the K_S, G, ρ, V_P, and V_S, whereas Fe decreases G, V_P, Vs but increases the K_S and ρ (Fig. 4).

3.3. The effects of water, Fe, and pressure on intrinsic anisotropy of wadsleyite

Our data suggest that the incorporation of water in wadsleyite reduces its intrinsic anisotropy monotonically (Fig. 5, Table 3). However, increasing Fe# of wadsleyite decreases A^U, A^{Vp}, and D^{Vs} monotonically but its effect on A^{Vs} depends on the water content and pressure (Fig. 5). For example, A^{Vs} for dry wadsleyite at 15 GPa decreases with Fe# from 0 to ~3, then increases with Fe# from ~3 to 15. Pressure decreases the anisotropy of wadsleyite significantly through most of the investigated pressure range (Fig. 5). Increasing pressure from ambient condition to 15 GPa would reduce A^{Vp}, A^{Vs}, and D^{Vs} of wadsleyite by 40-50% (Table 3).

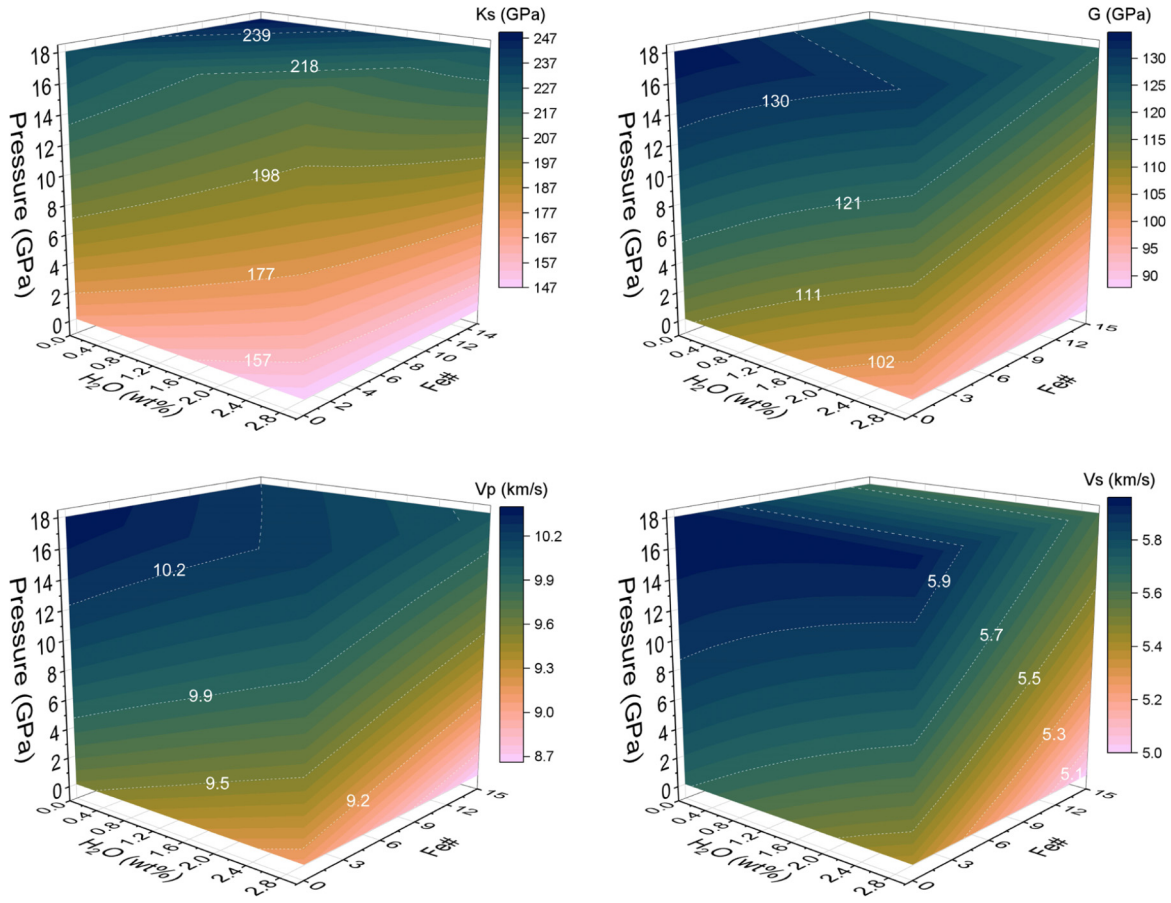

Fig. 4. The water, Fe, and pressure–dependent Ks, G, V_P, and V_S of isotropic polycrystalline wadsleyite aggregates under VRH averaging scheme (the batlow color scale is from Crameri, 2020).

Table 3
Average decrease of the elastic anisotropy caused by 1) increasing pressure from 0 to 15 GPa 2) adding 1 wt% water at 15 GPa and 300 K 3) increasing Fe# by 10 at 15 GPa and 300 K.

	1) Increase Pressure from 0 GPa to 15 GPa	2) Add 1 wt% water (at 15 GPa, 300 K)	3) Increase Fe# by 10 (at 15 GPa, 300 K)
A^U	↓ by ~72%	↓ by ~25%	↓ by ~19%
A^{Vp}	↓ by ~50%	↓ by ~13%	↓ by ~8%
A^{Vs}	↓ by ~49%	↓ by ~13%	↓ by ~13%
D^{Vs}	↓ by ~40%	↓ by ~11%	↓ by ~11%

4. Discussion

4.1. Compositional dependent elastic properties of single-crystal wadsleyite

To understand how water, Fe, and pressure influence acoustic velocities along different crystallographic directions of wadsleyite, we plotted the acoustic velocity surfaces for different single-crystal wadsleyite compositions derived from our water-Fe-pressure dependent single-crystal elasticity model using the MTEX software package (Mainprice et al., 2011).

For Fe-free dry wadsleyite at ambient condition (Fig. 6a), the fastest V_P is along [0 1 0] direction whereas the slowest V_P is along [0 0 1], because C_{22}>C_{11}>C_{33}. The fastest and slowest Vs propagation directions are along [0.6930 0.7199 0.0372] and [-0.5439 -0.4842 -0.6853] directions, which are close to [1 1 0] and [1 1 1] direction, respectively. The maximum V_S splitting direction is along [-0.5690 -0.6175 -0.5431], close to the direction of the slowest V_S propagation direction [1 1 1]. The velocity maximum and minimum directions for both V_P and V_S are insensitive to pressure (Fig. 6a and 6b).

After incorporating 1.5 wt% water to the Fe-free wadsleyite at 15 GPa (Fig. 6b and 6c), the fastest direction changes from [0 1 0] to [1 0 0] and the maximum V_P value drops from 10.9 km/s to 10.8 km/s. This is caused by the greater reduction of C_{22} than C_{11} caused by water. On the contrary, the slowest V_P value (9.9 km/s) and direction ([0 0 1]) remain almost the same after adding water in the crystal structure because C_{33} is relatively insensitive to water. Therefore, adding water decreases A^{Vp}. The higher sensitivity of C_{22} to water content compared with C_{33} is consistent with the fact that the unit cell parameters b and c are the most and least sensitive parameters to the water content, respectively (Holl et al., 2008; Buchen et al., 2017). On the other hand, the fastest V_S direction remains unchanged with higher water content, and the slowest V_S direction changes to [0 0 1] for hydrous wadsleyite (Fig. 6b and 6c).

With Fe# of wadsleyite changing from 0 to 10, the fastest and slowest V_P directions as well as the fastest Vs direction remain almost unchanged (Fig. 6b and 6d). However, the slowest V_S direction changes from [1 1 1] to [0 0 1]. Fe decreases the A^{Vp} because Fe affects C_{22} more than C_{33} (Fig. S6).

4.2. Seismic properties of deformed wadsleyite aggregates

Combining our modeled water-Fe-pressure dependent $C_{ij}s$ with the experimentally determined deformation-induced LPOs of wadsleyite aggregates from Ohuchi et al. (2014), we calculated the

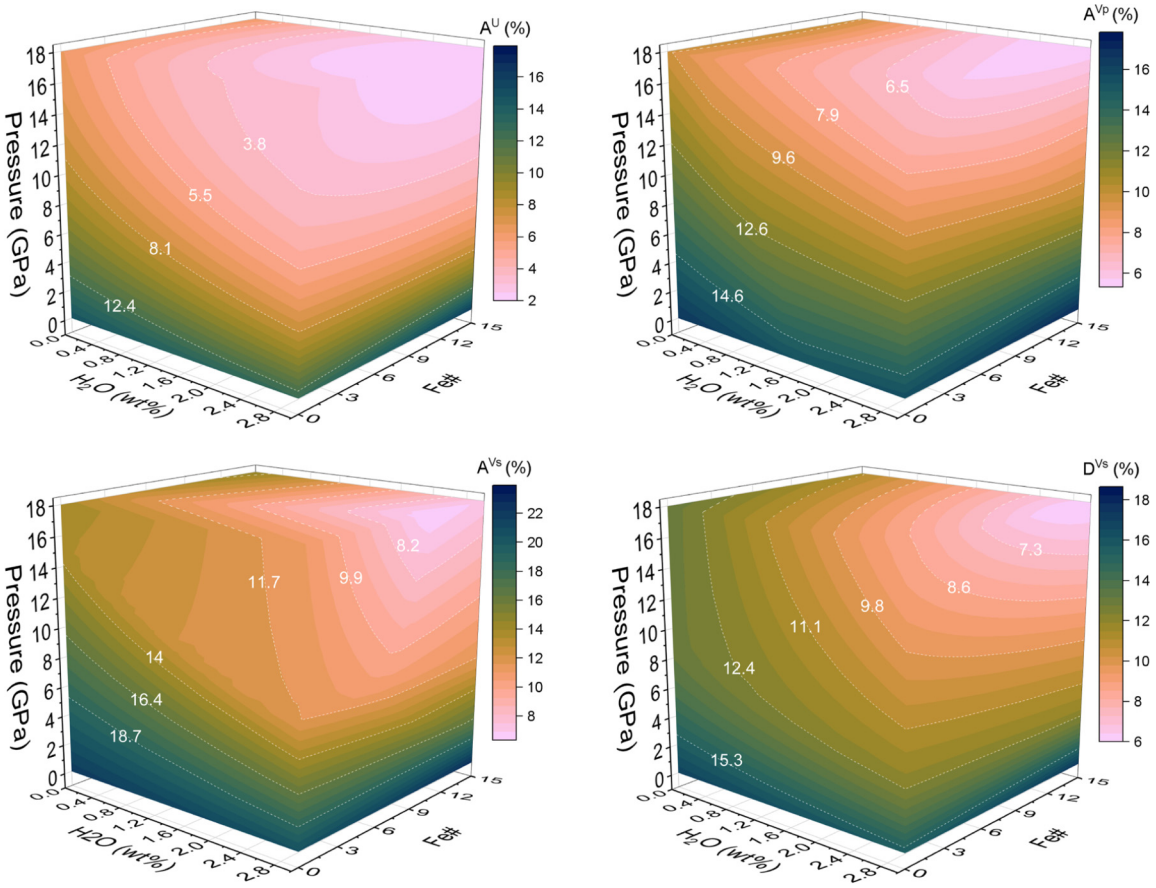

Fig. 5. The water, Fe, and pressure–dependent intrinsic anisotropy of single-crystal wadsleyite. A^{U} is universal anisotropy, A^{Vp} is Vp azimuthal anisotropy, A^{Vs} is Vs azimuthal anisotropy, D^{Vs} is radial anisotropy.

anisotropic seismic properties of deformed wadsleyite aggregates utilizing the MTEX software package (Fig. 7). The $C_{ij}s$ of wadsleyite used here are calculated at 15 GPa 300 K due to the lack of high pressure-temperature single-crystal elasticity measurements of wadsleyite. The deformation-induced LPOs of wadsleyite aggregates are measured by Electron Back Scattering Diffraction in Ohuchi et al., 2014, including sample M0327 for the type I [0 0 1] (0 1 0) fabric, sample M0310 for the type II [0 0 1] (1 0 0) fabric, samples Y0313 and M0308 for the type III fabric [1 0 0] (0 0 1). The type-II and type-III LPOs presented in Ohuchi et al. (2014) are based on deformation experiments on hydrous wadsleyite aggregates with water content limited to 0.3 wt%. The updated anisotropy modeling results using the $C_{ij}s$ model in this study for wadsleyite with 0.3 wt% water are shown in Fig. S8. However, in a hydrated mantle near subduction zones, the water content in wadsleyite might be higher than that considering the relatively large amount of water supply and the low-temperature condition in the subduction zones (Bercovici and Karato, 2003). Therefore, as an extreme end member case, we performed the anisotropy modeling on hydrous wadsleyite aggregates containing ~1.5 wt% water, under the assumption that they would develop the same fabrics as the less hydrated wadsleyite aggregates used in Ohuchi et al. (2014) (Fig. 7).

Under the normal upper MTZ temperatures (~1800 K), type-I and type-II fabrics of wadsleyite are more likely to develop with [0 0 1] axis of wadsleyite sub-parallel to the shear direction (Ohuchi et al., 2014). As discussed in section 4.1, [0 0 1] is always the slowest V_P direction of wadsleyite which is unlikely to be influenced by the water or Fe contents, so both the dry wadsleyite aggregate with type-I fabric and hydrous wadsleyite aggregate with type-II fabric show the slowest V_P direction along the shear direction (Fig. 7). Under lower temperatures (1473-1713 K), type III fabric is developed with [1 0 0] axis of wadsleyite parallel to the shear direction (Ohuchi et al., 2014). [1 0 0] is a fast V_P direction for dry wadsleyite and the fastest one for hydrous wadsleyite, so both dry wadsleyite aggregate and hydrous wadsleyite aggregate with type-III fabric show the fastest V_P direction sub-parallel to the shear direction.

Constraining V_{SH} (horizontally polarized shear wave velocity)/ V_{SV} (vertically polarized shear wave velocity) for wadsleyite aggregates under a vertical flow or a horizontal flow can help us understand the mantle flow field based on seismic observations. Higher mode surface waves have been used by seismic studies to constrain the V_{SH}/V_{SV} in the MTZ (Panning and Romanowicz, 2006; Visser et al., 2008). The polarization of V_{SV} is sub-perpendicular to the Earth's surface and the polarization of V_{SH} is sub-parallel to the Earth's surface (Fig. S7). In this study, we assumed V_{S1} is the fast V_S and V_{S2} is the slow V_S propagating along the same direction. For wadsleyite aggregates developing type-I and -II fabrics under normal MTZ temperatures (Fig. 7a, 7b), V_{S1} is V_{SV} assuming a horizontal mantle flow field while V_{S1} is V_{SH} in a vertical mantle flow field (Fig. S7). Therefore, wadsleyite aggregate with type-I and -II fabrics results in $V_{SV} > V_{SH}$ in a horizontal flow field, whereas $V_{SV} < V_{SH}$ is expected in a vertical flow field. Visser et al. (2008) and French and Romanowicz (2014) both suggested $V_{SV} > V_{SH}$ as a global feature in the MTZ, which is consistent with the Type-I and -II fabrics of wadsleyite developed under the normal MTZ temperatures in a horizontal flow field. Therefore, the flow field in the MTZ on the global scale is likely to be dominated by a horizontal flow (Ohuchi et al., 2014). This conclusion also coincides with the

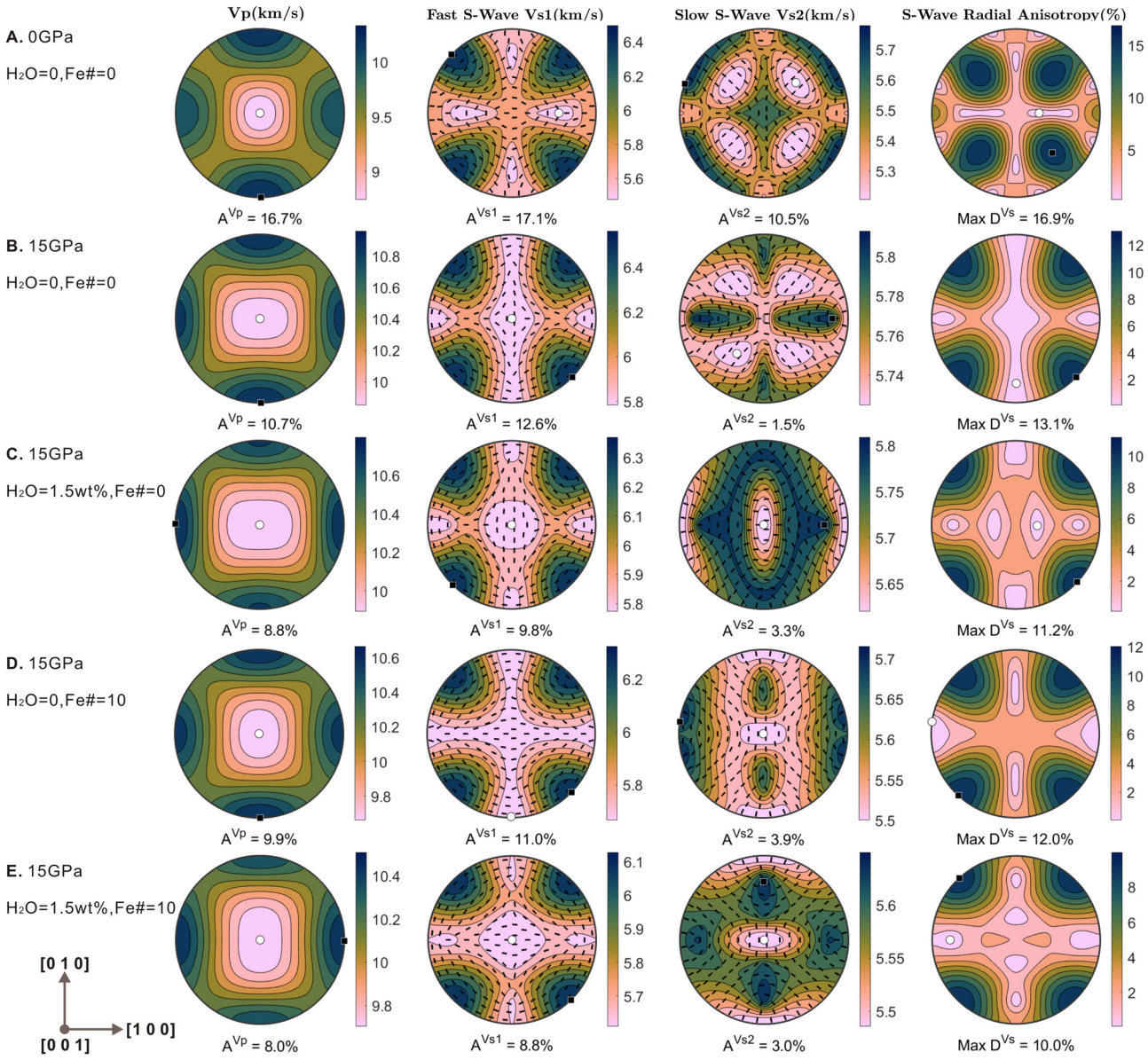

Fig. 6. Acoustic velocities along different crystallographic directions in stereographic projections for (A) dry wadsleyite with Fe#=0 at 0 GPa, (B) dry wadsleyite with Fe#=0 at 15 GPa, (C) hydrous wadsleyite with Fe#=0 at 15 GPa, (D) dry wadsleyite with Fe#=10 at 15 GPa, (E) hydrous wadsleyite with Fe#=10 at 15 GPa. Black and white dots represent the positions of the maximum and minimum velocities, respectively; The black short lines in fast S-wave V_{S1} and slow S-wave V_{S2} plots indicate the polarization directions. The crystallographic axes are shown in the bottom left corner. A^{Vp}, A^{Vs1} and A^{Vs2} refer to the maximum anisotropy values.

eastward horizontal mantle flow down to 700 km depth suggested by the observed global subduction asymmetry (steep westward subduction angle ~65° versus gentle eastward subduction angle ~27°, Ficini et al., 2017).

For wadsleyite aggregates with type-III fabric under cold conditions (Fig. 7c, 7d), we expect $V_{SV} < V_{SH}$ in a horizontal flow field and $V_{SV} > V_{SH}$ in a vertical flow field. $V_{SV} > V_{SH}$ has been reported to be associated with subducted slabs in the MTZ in locations such as the Western Pacific (Panning and Romanowicz, 2006; Chang and Ferreira, 2019), Central America (Panning and Romanowicz, 2006), and South America (Moulik and Ekström, 2014). This is consistent with the primarily vertical flow fields in the MTZ induced by subducted slabs suggested by the present study. However, some caution is warranted regarding the association of seismically imaged slabs in the MTZ and radial anisotropy given that actual flow directions can deviate from an exactly vertical orientation and not all hypothesized slabs in the MTZ exhibit $V_{SV} > V_{SH}$.

5. Implications

5.1. Anisotropy features in the MTZ

The magnitude of the azimuthal shear wave anisotropy A^{Vs} in the MTZ is controversial. It is constrained to be 0.8-1.1% by Yuan and Beghein (2013, 2018), 0.3-0.4% by Schaeffer et al. (2016), and 0.7-0.8% by Debayle et al. (2016). As suggested by Huang et al. (2019), the amplitude of azimuthal shear wave anisotropy A^{Vs} in the global upper mantle above the 410-km discontinuity is constrained to be ~1-2%, but this value in the MTZ drops to less than 1%, which is consistent with the significantly smaller intrinsic anisotropy of wadsleyite compared with olivine (Zhang et al., 2018). As shown in section 4.2, the A^{Vs} of wadsleyite aggregates with type I and type II fabrics is calculated to be only 0.6-0.9% under ambient MTZ conditions (Fig. 7). Considering that wadsleyite may make up ~60 vol% of the ambient mantle (Frost, 2008), the resulting anisotropy in the MTZ would be at the level of only ~0.4-

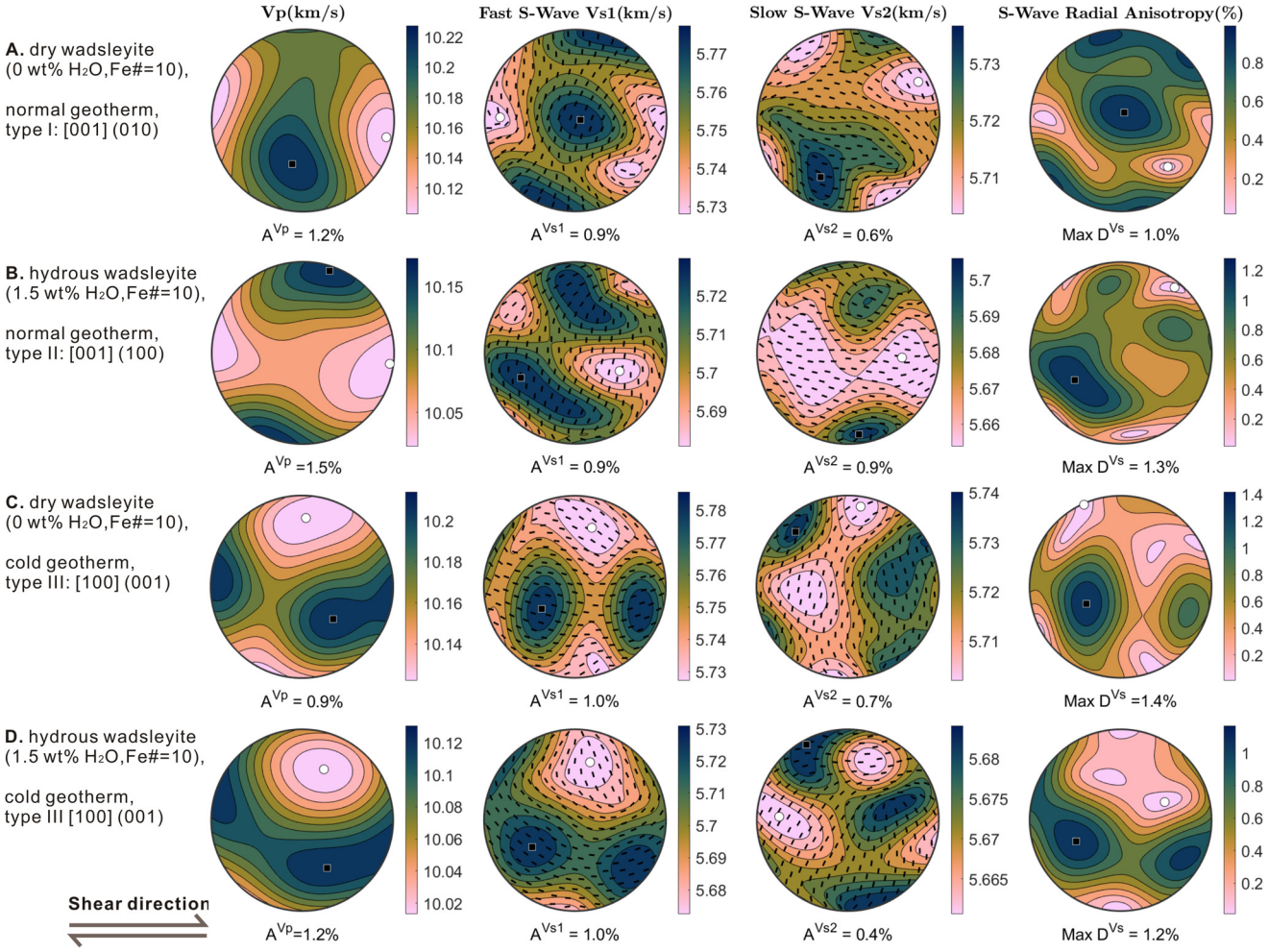

Fig. 7. The calculated acoustic velocities in stereographic projections for (A) dry wadsleyite aggregate with type I LPO (M0327), (B) hydrous wadsleyite aggregate with type II LPO (M0310), (C) dry wadsleyite aggregate with type III LPO (Y0313), (D) hydrous wadsleyite aggregate with type III LPO (M0308). The LPO data are from Ohuchi et al. (2014). The shear plane normal is north-south. The geometrical relationship between V_{SV} and V_{SH} is shown in Fig. S7. A^{Vp}, A^{Vs1} and A^{Vs2} refer to the maximum anisotropy values.

0.5%, which is more consistent with the estimates of Schaeffer et al. (2016), Debayle et al. (2016) and Huang et al. (2019).

The amplitude for the radial anisotropy D^{Vs} above the 410-km discontinuity is about 2%, but this value drops to ~1% below the 410-km discontinuity (Visser et al., 2008). In a pyrolitic mantle, the D^{Vs} caused by deformed wadsleyite with type-I and -II fabrics is only ~0.6-0.8%. A pyrolitic layer of 100 km thickness in the upper MTZ (~410-520 km) produces very short delay time (S-wave splitting time < 0.1 s) regardless of the types of LPO fabrics or water content in wadsleyite assumed. This is consistent with the negligible depth dependence of shear-wave splitting delay times obtained from deep earthquakes (Mohiuddin et al., 2015). The weak radial anisotropy in the global MTZ is well-explained by the weak radial anisotropy of deformed wadsleyite aggregates.

Near subducted slabs in the MTZ, the A^{Vs} and D^{Vs} can reach 2-3% locally beneath the circum-Pacific Ocean subduction zones (Huang et al., 2019; Moulik and Ekstrom, 2014). However, for wadsleyite developing type-III fabric along cold subduction geotherm, the pure wadsleyite aggregate shows a maximum A^{Vs} and D^{Vs} on the order of only 1-1.4% (Fig. 7). It is possible that the total strain in the MTZ induced by the subduction of cold slabs is significantly higher than strain achieved in the laboratory deformation experiment (0.6-1.1) by Ohuchi et al. (2014). Stronger LPO of wadsleyite may lead to the higher seismic anisotropy suggested by these local seismic studies. Some other studies have attributed the marked anisotropy underneath the subduction zones to the LPO of highly anisotropic hydrous alphabet phases (Nowacki et al., 2015) or K-hollandite (Mookherjee and Steinle-Neumann, 2009) in the subducted slabs. However, the stability and abundance of alphabet phases in the subducting slabs remain controversial and K-hollandite may only be present within subducted continental materials (Hao et al., 2020). Kawakatsu and Yoshioka (2011) identified a wedge-shape low-velocity layer in the subducting Pacific slab up to 450 km depth beneath SE Japan and explained it as the metastable olivine wedge. Tono et al. (2009) also reported a uniform anisotropy signal of the Pacific slab beneath Japan likely at depths beyond the 410-discontinuity. Considering the relatively high elastic anisotropy of olivine at 410 km (~19–25%, Zhang et al., 2018), the existence of metastable olivine in MTZ can explain the ~3% anisotropy associated with some cold subduction zones. Other possibilities include the highly anisotropic akimotoite (Shiraishi et al., 2008) and stishovite (Xu et al., 2020) accumulated in the stagnant slabs in the MTZ or shape-preferred orientation (SPO) of rheologically/elastically weak minerals/melts (Li et al., 2018). Deformed pure akimotoite aggregates show 3-4.3% A^{Vp} under the strain of 0.09-0.61 (Shiraishi et al., 2008), much higher than the deformed pure wadsleyite aggregates (~1%) and pure ringwoodite aggregates (~0.2%) under similar strain condition (Ohuchi et al., 2014). Foley and Long (2011) suggested that the main anisotropy contribution to splitting from deep earthquakes may come from

stagnant slabs at the boundary between the MTZ and the Lower Mantle, in which stishovite and akimotoite is likely to be locally enriched. A recent seismic study suggested that the non-double-couple deep earthquakes are probably originated in regions that are highly anisotropic (up to 25%) within the subducting slabs (Li et al., 2018), such high seismic anisotropy is difficult to be caused by LPO of elastically anisotropic mantle minerals, thus SPO seems a more viable explanation.

5.2. Is the seismic anisotropy in the upper MTZ a good water sensor?

A recent seismic study by Chang and Ferreira (2019) proposed a nearly dry upper MTZ (<~0.02 wt% water) near subducting slabs under the western Pacific due to the observed high radial anisotropy (~l.5%), and suggested that the high seismic anisotropy of the upper MTZ may indicate a low water content. It is interesting to reevaluate this conclusion based on our results that separate the pressure, Fe and water content effects and take various types of wadsleyite fabrics into account.

As shown in Fig. 5, water indeed reduces the intrinsic anisotropy of wadsleyite, for example, the A^{Vp} and D^{Vs} of hydrous wadsleyite (1.5 wt% water, Fe#=10) are lower than dry wadsleyite (Fe#=10) by 18% and 15%, respectively (Fig. 6d, 6e). However, the deformed hydrous wadsleyite aggregate usually shows type II fabric, whereas the deformed dry wadsleyite aggregate primarily displays type I fabric (Ohuchi et al., 2014). After taking the different types of fabrics into account, the hydrous wadsleyite actually shows higher A^{Vp} and D^{Vs} than the dry wadsleyite aggregate by 25% and 30%, respectively (Fig. 7a, 7b). A possible reason is that the incorporation of water results in more structural defects and assists the formation of stronger LPO of high-pressure olivine polymorphs such as wadsleyite and ringwoodite. As shown in Ohuchi et al. (2014), hydrous wadsleyite aggregate with type II fabric shows almost 2 times higher strain rate (~$1.3^{*}10^{-4}$) than the almost dry wadsleyite aggregate (~$7.4^{*}10^{-5}$) with type I fabric, thus the hydrous wadsleyite aggregate is rheologically weaker. Similarly, Kavner (2003) also reported that the presence of water in the crystal structure of ringwoodite increases the ductile strain rate, and thus, promotes the development of LPO of ringwoodite. Although the hydrous wadsleyite aggregate tends to show higher seismic anisotropy than the dry aggregate after taking the single-crystal elasticity and fabrics into account, whether this anisotropy difference can be resolved seismically will likely depend on the actual strain thus the strength of the flow field in the MTZ. Therefore, the seismic anisotropy in the upper MTZ may not necessarily reflect the degree of hydration in the MTZ.

6. Conclusions

(1) We determined the single-crystal elastic properties of a synthetic hydrous Fe-bearing wadsleyite (0.14 (4) wt% water, Fe#=9.4, $Fe^{3+}/\Sigma Fe$=0.3) up to 18.2 (2) GPa. The experimental results are: K_{S0} = 165 (2) GPa, G_0 = 104 (2) GPa, K_{S0}' = 5.2 (5), K_{S0}'' = -0.16 (11) GPa^{-1}, G_0' = 1.9 (2), and G_0'' = -0.076 (28) GPa^{-1}. Strong softening of C_{44} and C_{12} at pressures higher than 8 GPa is not observed in this study.

(2) We quantitively constrained the influence of water, Fe, and pressure on single-crystal elastic properties and intrinsic anisotropy of wadsleyite. In average, adding 1 wt% water into wadsleyite crystal structure at 15 GPa decreases intrinsic anisotropy by ~11-13%, adding 10 mol% Fe at 15 GPa decreases intrinsic anisotropy by ~8-11%, increasing pressure from 0 to 15 GPa decreases intrinsic anisotropy by ~40-50%.

(3) Utilizing the water-Fe-pressure dependent C_{ij} models of wadsleyite in the present study and 3 different types of fabrics measured by deformation experiments in Ohuchi et al. (2014), we modeled the seismic anisotropy of wadsleyite aggregates. Comparisons between our results and seismic observations in the MTZ suggest sub-horizontal flow in the ambient mantle and sub-vertical flow near subducted slabs. Our results are consistent with a weak anisotropic MTZ (<1%) on the global scale. The observed local high seismic anisotropy up to 3% near subducted slabs requires either high strain caused by strong flow fields, or the LPO of other strongly anisotropic minerals such as akimotoite, stishovite, and metastable olivine near the slabs.

(4) Water in wadsleyite's crystal structure decreases its intrinsic anisotropy but promotes the development of LPO. Depending on the total accumulated strain in the MTZ, the seismic anisotropy in the upper MTZ may not necessarily reflect the degree of hydration in the MTZ.

Declaration of competing interest

The authors declare that they have no known competing financial interests or personal relationships that could have appeared to influence the work reported in this paper.

Acknowledgement

We thank Mike Spilde for his general help in the EPMA analysis, Dr. Ruijia Wang for discussion of seismic ray paths, and Sibo Chen for the advice in the FTIR measurement. This project is funded by NSF-EAR-1664471 (JSZ). B.C. acknowledges the support from NSF-EAR-1555388 and NSF-EAR-1829273. LM acknowledges the support from NSF-EAR-1654687. Use of 13-BM-C was supported by COMPRES under NSF Cooperative Agreement EAR-1661511 and by GSECARS through NSF grant EAR-1634415 and DOE grant DE-FG02-94ER14466. Use of the APS was supported by the US Department of Energy, Office of Science, Office of Basic Energy Sciences, under Contract No. DE-AC02-06CH11357.

Appendix A. Supplementary material

Supplementary material related to this article can be found online at https://doi.org/10.1016/j.epsl.2021.116955.

References

Bercovici, D., Karato, S.I., 2003. Whole-mantle convection and the transition-zone water filter. Nature 425 (6953), 39–44. https://doi.org/10.1038/nature01918.

Buchen, J., Marquardt, H., Ballaran, T.B., Kawazoe, T., McCammon, C., 2017. The equation of state of wadsleyite solid solutions: constraining the effects of anisotropy and crystal chemistry. Am. Mineral. 102 (12), 2494–2504. https://doi.org/10.2138/am-2017-6162.

Buchen, J., Marquardt, H., Speziale, S., Kawazoe, T., Ballaran, T.B., Kurnosov, A., 2018. High-pressure single-crystal elasticity of wadsleyite and the seismic signature of water in the shallow transition zone. Earth Planet. Sci. Lett. 498, 77–87. https://doi.org/10.1016/j.epsl.2018.06.027.

Chang, S.J., Ferreira, A.M., 2019. Inference on water content in the mantle transition zone near subducted slabs from anisotropy tomography. Geochem. Geophys. Geosyst. 20 (2), 1189–1201. https://doi.org/10.1029/2018GC008090.

Chang, Y.Y., Jacobsen, S.D., Bina, C.R., Thomas, S.M., Smyth, J.R., Frost, D.J., et al., 2015. Comparative compressibility of hydrous wadsleyite and ringwoodite: effect of H2O and implications for detecting water in the transition zone. J. Geophys. Res., Solid Earth 120 (12), 8259–8280. https://doi.org/10.1002/2015JB012123.

Crameri, F., 2020. Scientific colour maps. http://www.fabiocrameri.ch/colourmaps.

Davies, G.F., Dziewonski, A.M., 1975. Homogeneity and constitution of the Earth's lower mantle and outer core. Phys. Earth Planet. Inter. 10 (4), 336–343. https://doi.org/10.1016/0031-9201(75)90060-6.

Debayle, E., Dubuffet, F., Durand, S., 2016. An automatically updated S-wave model of the upper mantle and the depth extent of azimuthal anisotropy. Geophys. Res. Lett. 43 (2), 674–682. https://doi.org/10.1002/2015GL067329.

Dyar, M.D., Agresti, D.G., Schaefer, M.W., Grant, C.A., Sklute, E.C., 2006. Mössbauer spectroscopy of Earth and planetary materials. Annu. Rev. Earth Planet. Sci. 34, 83–125. https://doi.org/10.1146/annurev.earth.34.031405.125049.

Ficini, E., Dal Zilio, L., Doglioni, C., Gerya, T.V., 2017. Horizontal mantle flow controls subduction dynamics. Sci. Rep. 7 (1), 1–7. https://doi.org/10.1038/s41598-017-06551-y.

French, S.W., Romanowicz, B.A., 2014. Whole-mantle radially anisotropic shear velocity structure from spectral-element waveform tomography. Geophys. J. Int. 199 (3), 1303–1327. https://doi.org/10.1093/gji/ggu334.

Frost, D.J., 2008. The upper mantle and transition zone. Elements 4 (3), 171–176. https://doi.org/10.2113/GSELEMENTS.4.3.171.

Foley, B.J., Long, M.D., 2011. Upper and mid-mantle anisotropy beneath the Tonga slab. Geophys. Res. Lett. 38 (2). https://doi.org/10.1029/2010GL046021.

Hazen, R.M., Weinberger, M.B., Yang, H., Prewitt, C.T., 2000. Comparative high-pressure crystal chemistry of wadsleyite, β-(Mg1−xFex)2SiO4, with x = 0 and 0.25. Am. Mineral. 85 (5–6), 770–777. https://doi.org/10.2138/am-2000-5-617.

Hao, M., Zhang, J.S., Pierotti, C.E., Zhou, W.Y., Zhang, D., Dera, P., 2020. The seismically fastest chemical heterogeneity in the Earth's deep upper mantle—implications from the single-crystal thermoelastic properties of jadeite. Earth Planet. Sci. Lett. 543, 116345. https://doi.org/10.1016/j.epsl.2020.116345.

Hill, R., 1963. Elastic properties of reinforced solids: some theoretical principles. J. Mech. Phys. Solids 11 (5), 357–372. https://doi.org/10.1016/0022-5096(63)90036-X.

Holl, C.M., Smyth, J.R., Jacobsen, S.D., Frost, D.J., 2008. Effects of hydration on the structure and compressibility of wadsleyite, β-(Mg2SiO4). Am. Mineral. 93 (4), 598–607. https://doi.org/10.2138/am.2008.2620.

Huang, Q., Schmerr, N., Waszek, L., Beghein, C., 2019. Constraints on seismic anisotropy in the mantle transition zone from long-period SS precursors. J. Geophys. Res., Solid Earth 124 (7), 6779–6800. https://doi.org/10.1029/2019JB017307.

Inoue, T., Yurimoto, H., Kudoh, Y., 1995. Hydrous modified spinel, Mg1. 75SiH0. 5O4: a new water reservoir in the mantle transition region. Geophys. Res. Lett. 22 (2), 117–120. https://doi.org/10.1029/94GL02965.

Jacobsen, S.D., Jiang, F., Mao, Z., Duffy, T.S., Smyth, J.R., Holl, C.M., Frost, D.J., 2008. Effects of hydration on the elastic properties of olivine. Geophys. Res. Lett. 35 (14). https://doi.org/10.1029/2008GL034398.

Jiang, F., Speziale, S., Duffy, T.S., 2004. Single-crystal elasticity of grossular- and almandine-rich garnets to 11 GPa by Brillouin scattering. J. Geophys. Res., Solid Earth 109 (B10). https://doi.org/10.1029/2004JB003081.

Kavner, A., 2003. Elasticity and strength of hydrous ringwoodite at high pressure. Earth Planet. Sci. Lett. 214 (3–4), 645–654. https://doi.org/10.1016/S0012-821X(03)00402-3.

Kawakatsu, H., Yoshioka, S., 2011. Metastable olivine wedge and deep dry cold slab beneath southwest Japan. Earth Planet. Sci. Lett. 303 (1–2), 1–10. https://doi.org/10.1016/j.epsl.2011.01.008.

Li, J., Zheng, Y., Thomsen, L., Lapen, T.J., Fang, X., 2018. Deep earthquakes in subducting slabs hosted in highly anisotropic rock fabric. Nat. Geosci. 11 (9), 696–700. https://doi.org/10.1038/s41561-018-0188-3.

Mainprice, D., Hielscher, R., Schaeben, H., 2011. Calculating anisotropic physical properties from texture data using the MTEX open-source package. Geol. Soc. (Lond.) Spec. Publ. 360 (1), 175–192. https://doi.org/10.1144/SP360.10.

Mao, Z., Jacobsen, S.D., Frost, D.J., McCammon, C.A., Hauri, E.H., Duffy, T.S., 2011. Effect of hydration on the single-crystal elasticity of Fe-bearing wadsleyite to 12 GPa. Am. Mineral. 96 (10), 1606–1612. https://doi.org/10.2138/am.2011.3807.

Mao, Z., Jacobsen, S.D., Jiang, F., Smyth, J.R., Holl, C.M., Frost, D.J., Duffy, T.S., 2008a. Single-crystal elasticity of wadsleyites, β-Mg2SiO4, containing 0.37–1.66 wt.% H2O. Earth Planet. Sci. Lett. 266 (1–2), 78–89. https://doi.org/10.1016/j.epsl.2007.10.045.

Mao, Z., Jacobsen, S.D., Jiang, F., Smyth, J.R., Holl, C.M., Duffy, T.S., 2008b. Elasticity of hydrous wadsleyite to 12 GPa: implications for Earth's transition zone. Geophys. Res. Lett. 35 (21). https://doi.org/10.1029/2008GL035618.

Mohiuddin, A., Long, M.D., Lynner, C., 2015. Mid-mantle seismic anisotropy beneath southwestern Pacific subduction systems and implications for mid-mantle deformation. Phys. Earth Planet. Inter. 245, 1–14. https://doi.org/10.1016/j.pepi.2015.05.003.

Mookherjee, M., Steinle-Neumann, G., 2009. Detecting deeply subducted crust from the elasticity of hollandite. Earth Planet. Sci. Lett. 288 (3–4), 349–358. https://doi.org/10.1016/j.epsl.2009.09.037.

Moulik, P., Ekström, G., 2014. An anisotropic shear velocity model of the Earth's mantle using normal modes, body waves, surface waves and long-period waveforms. Geophys. J. Int. 199 (3), 1713–1738. https://doi.org/10.1093/gji/ggu356.

Nowacki, A., Kendall, J.M., Wookey, J., Pemberton, A., 2015. Mid-mantle anisotropy in subduction zones and deep water transport. Geochem. Geophys. Geosyst. 16 (3), 764–784. https://doi.org/10.1002/2014GC005667.

Núñez-Valdez, M., Da Silveira, P., Wentzcovitch, R.M., 2011. Influence of iron on the elastic properties of wadsleyite and ringwoodite. J. Geophys. Res., Solid Earth 116 (B12). https://doi.org/10.1029/2011JB008378.

Ohuchi, T., Fujino, K., Kawazoe, T., Irifune, T., 2014. Crystallographic preferred orientation of wadsleyite and ringwoodite: effects of phase transformation and water on seismic anisotropy in the mantle transition zone. Earth Planet. Sci. Lett. 397, 133–144. https://doi.org/10.1016/j.epsl.2014.03.066.

Panning, M., Romanowicz, B., 2006. A three-dimensional radially anisotropic model of shear velocity in the whole mantle. Geophys. J. Int. 167 (1), 361–379. https://doi.org/10.1111/j.1365-246X.2006.03100.x.

Ranganathan, S.I., Ostoja-Starzewski, M., 2008. Universal elastic anisotropy index. Phys. Rev. Lett. 101 (5), 055504. https://doi.org/10.1103/PhysRevLett.101.055504.

Savage, M.K., 1999. Seismic anisotropy and mantle deformation: what have we learned from shear wave splitting? Rev. Geophys. 37 (1), 65–106. https://doi.org/10.1029/98RG02075.

Sawamoto, H., Weidner, D.J., Sasaki, S., Kumazawa, M., 1984. Single-crystal elastic properties of the modified spinel (beta) phase of magnesium orthosilicate. Science 224 (4650), 749–751. https://science.sciencemag.org/content/224/4650/749.

Schaeffer, A.J., Lebedev, S., Becker, T.W., 2016. Azimuthal seismic anisotropy in the Earth's upper mantle and the thickness of tectonic plates. Geophys. Suppl. Mon. Not. R. Astron. Soc. 207 (2), 901–933. https://doi.org/10.1093/gji/ggw309.

Shiraishi, R., Ohtani, E., Kanagawa, K., Shimojuku, A., Zhao, D., 2008. Crystallographic preferred orientation of akimotoite and seismic anisotropy of Tonga slab. Nature 455 (7213), 657–660. https://doi.org/10.1038/nature07301.

Speziale, S., Duffy, T.S., 2002. Single-crystal elastic constants of fluorite (CaF 2) to 9.3 GPa. Phys. Chem. Miner. 29 (7), 465–472. https://doi.org/10.1007/s00269-002-0250-x.

Tono, Y., Fukao, Y., Kunugi, T., Tsuboi, S., 2009. Seismic anisotropy of the Pacific slab and mantle wedge beneath the Japanese islands. J. Geophys. Res., Solid Earth 114 (B7). https://doi.org/10.1029/2009JB006290.

Visser, K., Trampert, J., Lebedev, S., Kennett, B.L.N., 2008. Probability of radial anisotropy in the deep mantle. Earth Planet. Sci. Lett. 270 (3–4), 241–250. https://doi.org/10.1016/j.epsl.2008.03.041.

Wang, J., Bass, J.D., Kastura, T., 2014. Elastic properties of iron-bearing wadsleyite to 17.7 GPa: implications for mantle mineral models. Phys. Earth Planet. Inter. 228, 92–96. https://doi.org/10.1016/j.pepi.2014.01.015.

Xu, F., Yamazaki, D., Tsujino, N., Guan, L., 2020. Lattice preferred orientation of stishovite deformed at high pressure and high temperature. Phys. Earth Planet. Inter. 306, 106546. https://doi.org/10.1016/j.pepi.2020.106546.

Yuan, K., Beghein, C., 2013. Seismic anisotropy changes across upper mantle phase transitions. Earth Planet. Sci. Lett. 374, 132–144. https://doi.org/10.1016/j.epsl.2013.05.031.

Yuan, K., Beghein, C., 2018. A Bayesian method to quantify azimuthal anisotropy model uncertainties: application to global azimuthal anisotropy in the upper mantle and transition zone. Geophys. J. Int. 213 (1), 603–622. https://doi.org/10.1093/gji/ggy004.

Zha, C.S., Duffy, T.S., Mao, H.K., Downs, R.T., Hemley, R.J., Weidner, D.J., 1997. Single-crystal elasticity of β-Mg2SiO4 to the pressure of the 410 km seismic discontinuity in the Earth's mantle. Earth Planet. Sci. Lett. 147 (1–4), E9–E15. https://doi.org/10.1016/S0012-821X(97)00010-1.

Zhang, J.S., Bass, J.D., 2016. Sound velocities of olivine at high pressures and temperatures and the composition of Earth's upper mantle. Geophys. Res. Lett. 43 (18), 9611–9618. https://doi.org/10.1002/2016GL069949.

Zhang, J.S., Bass, J.D., Schmandt, B., 2018. The elastic anisotropy change near the 410-km discontinuity: predictions from single-crystal elasticity measurements of olivine and wadsleyite. J. Geophys. Res., Solid Earth 123 (4), 2674–2684. https://doi.org/10.1002/2017JB015339.